# Topology Optimization and Prototype of a Highly Adaptive Multi-Material Compliant Finger for Parallel Grippers

Chih-Hsing Liu, *Member, IEEE*, Yi-Chieh Shih, and Jui-Chih Chi

***Abstract*—Developing an adaptive robotic finger or gripping jaw capable of handling objects of diverse sizes and shapes presents a significant challenge in robotics. The fin ray-type compliant finger is one of the designs intended to adapt to the contours of a workpiece using passive compliance of its structure. However, according to our tests, the fin ray-type fingers only conform well to circular objects. In order to develop a highly adaptive finger design suitable for parallel grippers, we present a multi-material and multi-objective topology optimization method to synthesize an innovative compliant finger capable of conforming to circular, rectangular, concave, and asymmetric objects. The prototype of the multi-material compliant finger is manufactured via 3D printing using two different elastomers, and two identical fingers are installed on a parallel gripper actuator for grasping applications. The gripper's adaptability is determined based on the total contact length between its fingers and the object being grasped. The experimental results show that our novel multi-material parallel gripper outperformed the fin ray-type compliant gripper in both adaptability and maximum payload.**

***Index Terms*—Compliant mechanism, compliant gripper, parallel gripper, parallel-jaw gripper, soft robot, topology optimization.**

## I. Introduction

A PARALLEL gripper, or a parallel-jaw gripper, is a type of robotic end-effector typically comprising two opposing fingers or jaws that move in parallel to grasp and manipulate objects. Parallel grippers are widely used in industrial automation [1], [2], [3], [4] and play a crucial role in robotic systems, serving as the end-of-arm components of manipulators and directly interacting with the workpiece being handled. Developing an adaptive robotic finger or gripping jaw capable of handling objects of diverse sizes and shapes presents a significant challenge in robotics. To address this issue, various designs such as using biologically inspired concepts [5], [6], [7], [8], [9] and optimization methodologies [10], [11], [12], [13], [14], [15], [16], [17] are being explored.

Manuscript received 3 April 2024; accepted 25 July 2024. Date of publication 8 August 2024; date of current version 13 August 2024. This article was recommended for publication by Associate Editor M. Wehner and Editor Y. Park upon evaluation of the reviewers' comments. This work was supported by the Ministry of Science and Technology of Taiwan under Grant MOST 110-2628-E-006-004 and Grant MOST 111-2628-E-006-001-MY2. *(Corresponding author: Chih-Hsing Liu.)*

The authors are with the Department of Mechanical Engineering, National Cheng Kung University, Tainan 701, Taiwan (e-mail: chliu@mail.ncku.edu.tw).

This letter has supplementary downloadable material available at https://doi.org/10.1109/LRA.2024.3440837, provided by the authors.

Digital Object Identifier 10.1109/LRA.2024.3440837

The rapid progress in areas such as soft robotics, flexible electronics, and 3D printing, or additive manufacturing technology, in recent years has also driven the development of soft robotic grippers [18], [19]. Unlike traditional robots, which consist of rigid body mechanisms, the distinctive feature of soft robots is that their mechanisms, either partially or entirely, are composed of flexible components, also known as compliant mechanisms [20]. Typically, compliant mechanisms are monolithically formed, eliminating the need for additional joints or lubrication and resulting in relatively low manufacturing costs. For example, the fin ray-type adaptive finger [8], [9] is one kind of compliant mechanism inspired by a fish's tail fin. Moreover, soft pneumatic bending actuators [11], [12] and compliant grippers [10], [13], [14], [15], synthesized with topology optimization algorithms, have been developed specifically for grasping unknown objects.

Topology optimization is a computational technique used to iteratively optimize the material layout within a given design domain under specified constraints. Various optimization algorithms have been developed to synthesize compliant mechanisms [20] and structures [21]. Further, with the advancement of 3D printing technology, the topology optimization of multi-material compliant mechanisms is gradually gaining attention. For example, Gaynor et al. [22] utilized a multi-material topology optimization based on the Solid Isotropic Material with Penalization (SIMP) method [23] to design compliant inverter mechanisms. The prototypes were made by utilizing a PolyJet 3D printer capable of printing with two materials simultaneously. Experimental results showed that the multi-material design outperformed the single-material design, with approximately 1.8 times improvement in output displacement under a 9.65 kg load. To reduce computational costs, the ordered SIMP method [24], [25] was proposed to solve multi-material problems without introducing new variables.

The fin ray-type compliant finger [8], [9] is designed to adapt to the contours of an object using the passive compliance of its structure. However, according to our tests, the fin ray-type parallel gripper conforms well only to circular objects, leaving significant gaps when grasping other shapes, such as rectangular, concave, and asymmetric objects. Motivated by the need for an adaptive compliant gripping jaw for parallel grippers capable of handling objects of diverse sizes and shapes, this article presents an innovative multi-material compliant finger synthesized using a topology optimization method considering multi-material and multi-objective conditions. The prototypes of the multi-material

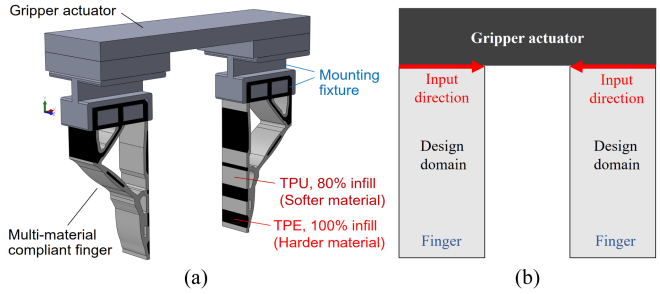


Fig. 1. Multi-material adaptive parallel gripper. (a) Design model. (b) Design domain for the compliant finger of the parallel gripper.

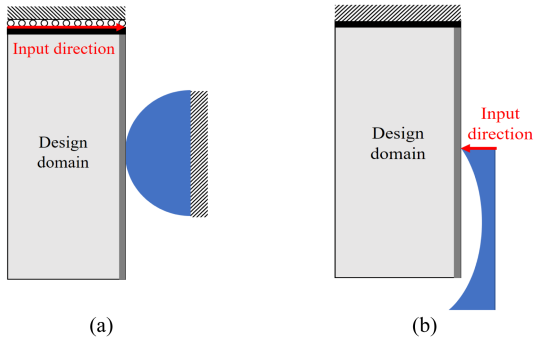


Fig. 2. Design schemes for the compliant finger of the adaptive parallel gripper (half symmetric model). (a) The design scheme for gripping a convex object. (b) The design scheme for gripping a concave object.

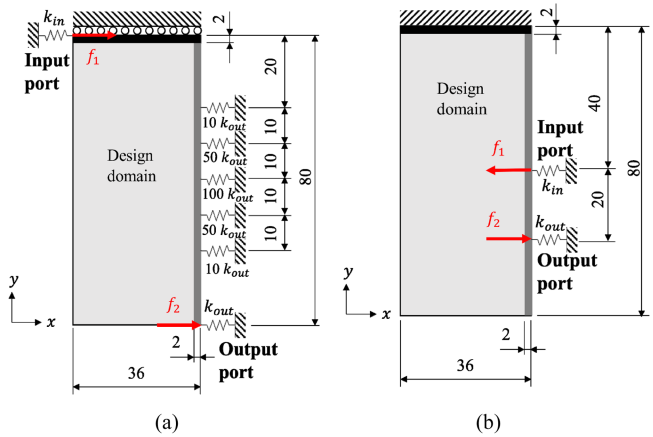


Fig. 3. Boundary conditions for topology optimization of the compliant finger. (a) Boundary condition for gripping the convex object (BC1). (b) Boundary condition for gripping the concave object (BC2).

compliant finger are manufactured through 3D printing using two distinct elastomers. These fingers are then installed on a parallel gripper actuator for grasping tasks. Experimental findings demonstrate that the novel multi-material parallel gripper outperforms the fin ray-type gripper in both adaptability and maximum payload by factors of 14.8 and 3.2, respectively, on average, among the tested objects.

## II. Multi-Material Adaptive Parallel Gripper

The design model of the innovative multi-material adaptive parallel gripper, presented in this study, is shown in Fig. 1(a). The parallel gripper comprises two identical multi-material compliant fingers mounted on a single gripper actuator through fixtures. As will be introduced in a later section, the geometry and the material distribution of the multi-material compliant finger is determined using a multi-material and multi-objective topology optimization algorithm. Fig. 1(b) shows the design domain for topology optimization of the compliant finger. During operation, the gripper actuator drives both fingers to move toward each other along a linear axis, facilitating the gripping of objects.

The multi-material compliant fingers are composed of two materials, thermoplastic elastomer (TPE) and thermoplastic polyurethane (TPU), and are manufactured using a fused deposition modeling (FDM) 3D printing process. The infill densities for 3D printing TPE and TPU are 100% and 80%, respectively. The TPE with 100% infill represents the harder material, whereas the TPU with 80% infill represents the softer material.

To enhance the gripper's adaptability, this study employs two design schemes to describe distinct gripping scenarios. The first design scheme, illustrated in Fig. 2(a), focuses on the condition of gripping convex objects. The concept involves assuming that the convex object remains fixed while the gripper finger moves to make contact with it. The second design scheme, presented in Fig. 2(b), is tailored for the condition of gripping concave objects, assuming that the object makes contact with the gripper finger. The reason for considering these two scenarios is to ensure that the designed finger is capable of gripping both convex and concave objects. In addition, objects with other shapes, such as asymmetric and rectangular objects, can be considered as combinations of convex and concave objects. Therefore, we use only two scenarios to simplify the optimization problem. Each gripping scenario in Fig. 2 assumes a symmetric boundary condition, which implies that the object and the gripper are positioned such that a vertical plane through the center of the object divides it and the gripper into two symmetric halves. Thus, half symmetric models can be used.

The design schemes in Fig. 2(a) and (b) can be converted into the boundary conditions illustrated in Fig. 3(a) and (b), respectively, for topology optimization. Here, $k_{in}$ and $k_{out}$ represent the stiffness of input and output springs, respectively, used for simulating external resistance; and $f_1$ and $f_2$ represent the input and output forces, respectively. The dimensions of the design domain for the compliant finger are 36 mm $\times$ 80 mm.

In the boundary condition for gripping the convex object (BC1), as illustrated in Fig. 3(a), the top region of the design domain is constrained in the y-direction due to its connection to the gripper actuator during operation. The upper left corner of the design domain is subjected to an input force $f_1$, simulating the input action of the gripper actuator. The top edge of the gripper finger is pre-specified with a 2 mm layer of the harder material. This ensures the efficient transfer of the input force to the gripping surface on the right side of the design domain. The gripping surface has a width of 2 mm and needs to be filled with materials, either harder or softer. Five numerical springs of different stiffness are added to the gripping surface to simulate different degrees of contact deformation when the gripper grips

the convex object. A virtual force $f_2$ is applied to the lower right corner of the design domain to represent the target output at the fingertip. The BC1 scheme will be used in the first design objective in the multi-objective topology optimization so that the optimized finger will be able to grip convex objects.

In the boundary condition for gripping the concave object (BC2), as illustrated in Fig. 3(b), the top region of the design domain represents the fixed end, simulating the gripper finger in contact with the concave object after gripping. Therefore, an input force $f_1$ is specified at the middle of the gripping surface. A virtual force $f_2$ is applied to the specified output port in Fig. 3(b) to accommodate the concave object. The BC2 scheme will be used in the second design objective in the multi-objective topology optimization, aiming to enable the optimized finger to effectively grip concave objects.

## III. Topology Optimization Method

The multi-objective optimization problem aims to maximize the mutual potential energy (MPE) of the synthesized multi-material compliant finger under BC1 and BC2, as illustrated in Fig. 3. The definition of MPE is as follows:

$$MPE = \mathbf{U}_2^T \mathbf{K} \mathbf{U}_1 \tag{1}$$

where $\mathbf{U}_2$ represents the global displacement vector corresponding to the output force vector $\mathbf{F}_2$ when only the output force $f_2$ is applied to the output port. $\mathbf{K}$ denotes the global stiffness matrix of the design domain, while $\mathbf{U}_1$ stands for the global displacement vector corresponding to the global input force vector $\mathbf{F}_1$ when only the input force $f_1$ is applied to the input port. These displacement vectors can be determined using the finite element method. Maximizing the MPE resulting from two different sets of loading enables a design to enhance its nodal displacement at the output port while applying the input force at the input port. Furthermore, a higher output displacement enhances the finger's ability to conform to the target object.

The multi-material topology optimization problem can be formulated as:

$$\begin{aligned} &\text{Min}: \quad \{-MPE_{BC1}, -MPE_{BC2}\} \\ &\text{Subject to}: \quad \mathbf{K}\mathbf{U}_1 = \mathbf{F}_1; \mathbf{K}\mathbf{U}_2 = \mathbf{F}_2 \\ &\sum_{e=1}^{N_e} v_e \breve{\rho}_e / \sum_{e=1}^{N_e} v_e = V^* \\ &0 \le \breve{\rho}_e \le 1 \end{aligned} \tag{2}$$

where $MPE_{\mathrm{BC1}}$ and $MPE_{\mathrm{BC2}}$ are MPE for the conditions of gripping convex and concave objects (BC1 and BC2), respectively; $N_e$ is the number of elements; $v_e$ is the volume of an element; $\breve{\rho}_e$ is the volumetric element density; and $V*$ is the target volume fraction after optimization.

A material interpolation scheme is presented as follows to deal with the multi-material problem.

$$E_e = E_i + \left( \frac{\bar{\rho}_e - \rho_i^{\mathrm{N}}}{\rho_{i+1}^N - \rho_i^{\mathrm{N}}} \right)^{p_i} (E_{i+1} - E_i), \bar{\rho}_e \in \left[ \rho_i^{\mathrm{N}}, \rho_{i+1}^N \right] \tag{3}$$

where $E_e$ represents the elastic modulus of the $e_{th}$ element; $E_i$ represents the elastic modulus of the $i_{th}$ material; $\bar{\rho}_e$ is the projected element density after projection, and its value ranges from 0 to 1; $p$ is a penalty parameter (greater than 1) used to achieve clear and distinct material distribution after penalization and can be estimated using an ordered SIMP interpolation method [24]; and $\rho_i^{\mathrm{N}}$ is the normalized material density of the $i_{th}$ material defined as:

$$\rho_i^{\mathrm{N}} = \frac{D_i}{D_{\max}}, i = 1, \ldots, m \tag{4}$$

where $D_i$ is the density of the $i_{th}$ material; $D_{max}$ is the largest density among the used materials; and $m$ is the number of materials (including the void material for void elements after optimization).

The projected element density $\bar{\rho}_e$ shown in (3) can be calculated using the presented multi-material projection scheme.

$$\bar{\rho}_e = \sum_{i=1}^{m-1} \left( \rho_{i+1}^N - \rho_i^N \right) \frac{\tanh\left(\beta \eta_i\right) + \tanh\left(\beta\left(\tilde{\rho}_e - \eta_i\right)\right)}{\tanh\left(\beta \eta_i\right) + \tanh\left(\beta(1 - \eta_i)\right)} \tag{5}$$

where $\beta$ is the projection parameter, and its initial value is set at 1. The value of $\beta$ will be doubled every 50$^{\text{th}}$ iterations until it reaches its maximum value, which is set at 512; $\eta_i$ is the threshold value of the $i_{th}$ material; and $\tilde{\rho}_e$ is the filtered density of the $e_{th}$ element that can be obtained using the following density filter:

$$\tilde{\rho}_e = \frac{\sum_{j \in N_e} w_{ej} v_j \rho_j}{\sum_{j \in N_e} w_{ej} v_j}, w_{ej} = \max(0, r_{\min} - r_{ej}) \tag{6}$$

where $w_{ej}$ is the weighted function; $r_{min}$ is the filter radius; $N_e$ represents the set of elements within the circular region with a radius of $r_{min}$ centered on the $e_{th}$ element; $v_j$ denotes the volume of the $j_{th}$ element; and $r_{ej}$ represents the distance between the $e_{th}$ element and the $j_{th}$ element.

In addition, the threshold value of the $i_{th}$ material in (5) can be defined as:

$$\eta_i = \frac{\rho_i^N + \rho_{i+1}^N}{2} \tag{7}$$

Similar to the projected element density, the volumetric element density in (2) can be defined as follows.

$$\breve{\rho}_e = \frac{\tanh(\breve{\beta}\eta_1) + \tanh(\breve{\beta}(\tilde{\rho}_e - \eta_1))}{\tanh(\breve{\beta}\eta_1) + \tanh(\breve{\beta}(1 - \eta_1))} \tag{8}$$

where $\breve{\beta}$ is the volumetric projection parameter.

Finally, the element sensitivity $\alpha_e$ can be calculated by taking the derivative of the objective function with respect to the design variable.

$$\alpha_e = \frac{\partial MPE}{\partial \rho_e} = \sum_{k \in N_e} \frac{\partial MPE}{\partial \bar{\rho}_k} \frac{\partial \bar{\rho}_k}{\partial \tilde{\rho}_k} \frac{\partial \tilde{\rho}_k}{\partial \rho_e} \tag{9}$$

where $\rho_e$ represents the element density of the $e_{\mathrm{th}}$ element, which acts as the design variable ranging from 0 to 1 with small increments during the optimization process. An element density of 1 indicates that the element should remain after optimization, while a density of 0 implies that the element should be removed.

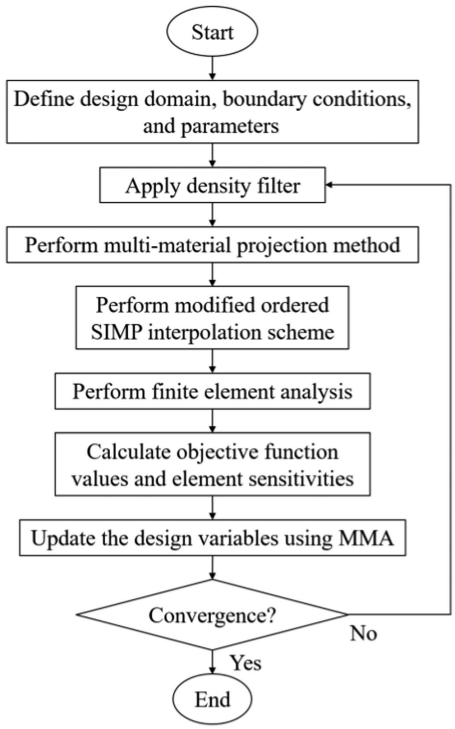


Fig. 4. Flowchart of the multi-material topology optimization procedure.

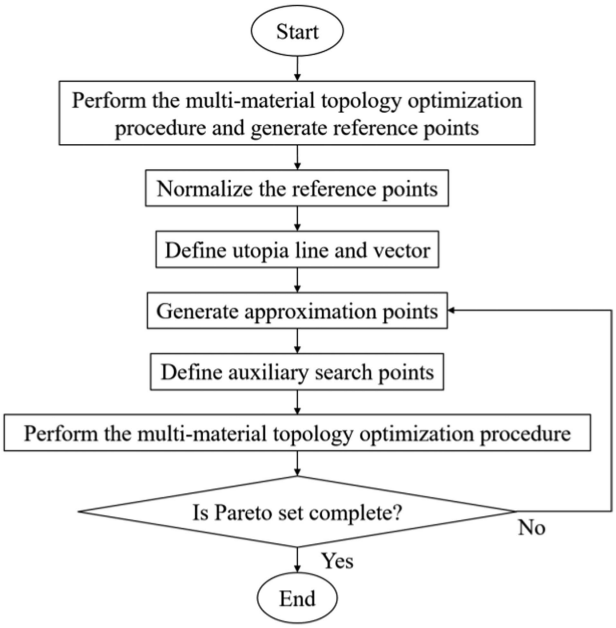


Fig. 5. Flowchart of the multi-objective topology optimization procedure.

The flowchart of the multi-material topology optimization procedure is shown in Fig. 4. The concept of robust topology optimization [26] is utilized to avoid one-node connected hinges. The design variables are updated by the method of moving asymptote (MMA) [27]. The flowchart of the multi-objective optimization procedure is depicted in Fig. 5. The multi-material topology optimization procedure outlined in Fig. 4 is separately executed using the first and second objective functions (based on BC1 and BC2, respectively) to obtain the individual optimal values. Then, based on the concept of the smart normal constraint method [28], [29], the original objective function value is normalized, transforming the multi-objective optimization problem into a series of single-objective optimization problems with additional constraints to produce a Pareto solution in a particular region. These constraints include two normal constraints and an auxiliary search constraint.

The optimization problem is defined as follows:

$$\begin{aligned}
&\text{Min}: \quad \mu_1(\boldsymbol{\rho}) \\
&\text{Subject to}: \quad \mathbf{K}\mathbf{U}_1 = \mathbf{F}_1; \mathbf{K}\mathbf{U}_2 = \mathbf{F}_2 \\
&\sum_{e=1}^{N_e} v_e \breve{\rho}_e / \sum_{e=1}^{N_e} v_e = V^* \\
&0 \le \boldsymbol{\rho} \le 1 \\
&N(\mu(\boldsymbol{\rho}) - S_l) \le 0; -N(\mu(\boldsymbol{\rho}) - S_r) \le 0 \\
&V_s(\mu(\boldsymbol{\rho}) - S) \le 0
\end{aligned} \tag{10}$$

where $\mu_1$ represents the first normalized objective; $\rho$ is the set of element densities; $N$ is the utopia line vector; $\mu$ denotes the normalized objective vector at the current iteration; $S_l$ and $S_r$ denote the points for the left and right normal constraints, respectively; $S$ is the approximation point; and $V_s$ is the vector for the auxiliary search constraint.

The convergence criteria involve tracking changes in element density, the objective function, and volume fraction. First of all, the change in each element density (*change*) needs to be less than or equal to a tolerance value, which is set as 0.01.

$$change = \max\left(|\boldsymbol{\rho}^{new} - \boldsymbol{\rho}|\right) \le 0.01 \tag{11}$$

where $\rho$ and $\rho^{new}$ are the element densities before and after the update, respectively.

The change in the objective function (*objchange*) is defined as:

$$objchange = \frac{mean\left(\sum_{n=1}^{5} |c_{loop-n+1} - c_{loop-n}|\right)}{|c_{loop}|} \le 0.005 \tag{12}$$

where *loop* is the iteration number in the topology optimization process; $c$ is the objective function value; and $c_{loop}$ represents the objective function value at the specific iteration (*loop*). To prevent *objchange* from being too small at the start of the topology optimization, it's value is set to 1 when loop$\le$10 and when the number of iterations under the same projection parameter $\beta$ in (5) is less than or equal to 5.

Finally, to ensure the volume fraction in (2) meets the target value $V*$ after optimization, the following volume fraction constraint needs to be satisfied.

$$\sum_{e=1}^{N_e} v_e \breve{\rho}_e / \sum_{e=1}^{N_e} v_e \le V^* \pm voltor \tag{13}$$

where *voltol* is the tolerance for the calculated volume fraction, which is set as 0.001.

TABLE I
NUMERICAL PARAMETERS USED IN THE TOPOLOGY OPTIMIZATION

| Parameter | Value |
|---|---|
| Element size | 0.5 mm |
| Design domain | 36 mm × 80 mm |
| Elastic modulus: void element ($E_1$) | $10^{-9}$ MPa |
| Elastic modulus: TPU 80% infill ($E_2$) | 14.73 MPa |
| Elastic modulus: TPE 100% infill ($E_3$) | 34.95 MPa |
| Normalized density : void element ($\rho_1$) | 0 |
| Normalized density : TPU 80% infill ($\rho_2$) | 0.746 |
| Normalized density : TPE 100% infill ($\rho_3$) | 1 |
| Poisson's ratio | 0.45 |
| Filtering radius ($r$) | 5 × element size |
| Penalty parameters ($p_1$ *and* $p_2$) | 3 and 2 |
| Projection parameter ($\beta$) | 1~512 |
| Volume fraction | 0.22 |
| Projection parameter for volume fraction ($\beta_v$) | $\beta$+1 |
| Threshold values ($\eta$) | 0.3, 0.5, 0.7 |
| Dummy input and output forces | 1 N |
| Spring stiffness for BC1 ($k_{in}$ *and* $k_{out}$) | 1 and 0.01 N/mm |
| Spring stiffness for BC2 ($k_{in}$ *and* $k_{out}$) | 1 N/mm |

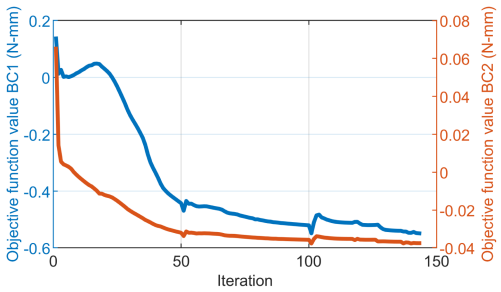


Fig. 6. Iterative objective function values for BC1 and BC2.

## IV. MULTI-MATERIAL FINGER DESIGN

The presented multi-material and multi-objective topology optimization procedures shown in Figs. 4 and 5, respectively, are used to synthesize the multi-material compliant finger for parallel grippers. The numerical parameters used in topology optimization are summarized in Table I, where the elastic moduli of the TPE with a 100% infill density and the TPU with an 80% infill density are 34.95 MPa [30] and 14.73 MPa, respectively, as obtained through tensile tests. The boundary conditions for the two objectives (gripping concave and convex objects as illustrated in Fig. 2) are shown in Fig. 3. The analysis domain is discretized using 72 × 160 two-dimensional, linear plane stress elements.

Fig. 6 shows the iterative results for the values of the two objective functions, illustrating the negative mutual potential energy minimization process. The blue curve and the left y-axis depict the objective function value for gripping the convex object (BC1), while the red curve and the right y-axis depict the objective function value for gripping the concave object (BC2). The iterative process converges after 144 iterations. The material layouts obtained during some iterations are presented in Fig. 7. The black-colored region represents the harder material (100% infill TPE) with an elastic modulus of 34.95 MPa, while the green-colored region represents the softer material (80% infill TPU) with an elastic modulus of 14.73 MPa. These two values are obtained based on the test results of the elastic moduli for the two 3D-printed elastomers. The white-colored region represents the void elements. The converged volume fraction values for the harder and softer materials in the analysis domain are 0.07 and 0.15, respectively.

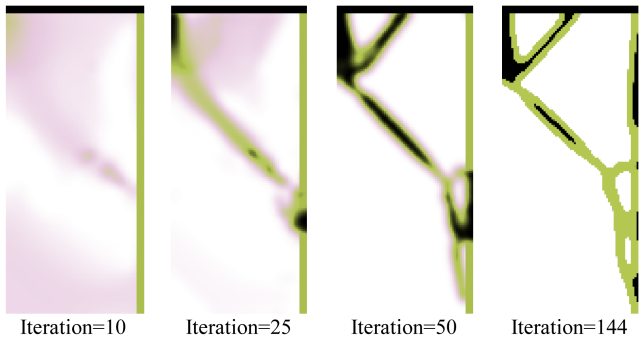


Fig. 7. Iterative topology optimization results of the compliant finger. The black-colored region represents the harder material (TPE with a 100% infill density, Elastic modulus = 34.95 MPa), while the green-colored region represents the softer material (TPU with an 80% infill density, Elastic modulus = 14.73 MPa).

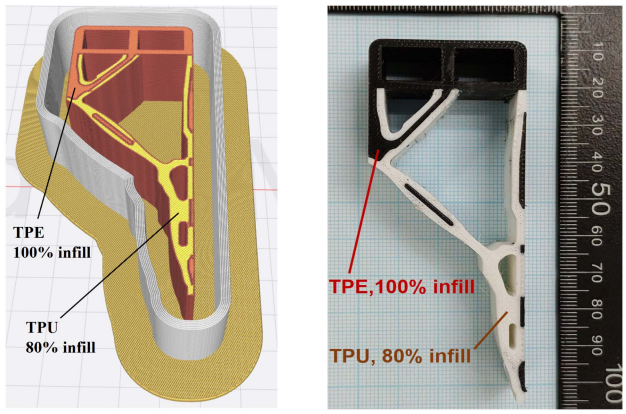


Fig. 8. Multi-material compliant finger. (a) The 3D printing model (b) the prototype of the multi-material compliant finger is printed with TPE with an infill density of 100% (representing the harder material) and TPU with an infill density of 80% (representing the softer material).

## V. PROTOTYPES AND EXPERIMENTAL RESULTS

The prototypes of the design for the multi-material compliant finger shown in Fig. 7 were fabricated using the Raise3D E2 3D printer. The commercial TPU filament, PolyFlex™, manufactured by Polymaker, and TPE filament, Filastic™, manufactured by BotFeeder, were utilized for the 3D printing process. The black-colored region in Fig. 7 represents the harder material and was printed using the TPE filament with a 100% infill density, while the green-colored region represents the softer material and was printed using the TPU filament with an infill density of 80%. The reason for using an 80% infill density for TPU is that its equivalent elastic modulus is approximately half that of TPE with a 100% infill rate, according to the results of our tensile tests. Fig. 8 shows the 3D printing model and the prototype of the multi-material compliant finger, both with a uniform thickness of 20 mm. The black and white materials in Fig. 8(b) are TPE and TPU, respectively. The manufacturing parameters for 3D

TABLE II
MANUFACTURING PARAMETERS FOR 3D PRINTING OF THE GRIPPER FINGER

| Parameter | Value |
|---|---|
| TPE Filament (BotFeeder Filastic™) | 100% infill |
| TPU Filament (Polymaker PolyFlex™) | 80% infill |
| Infill pattern | Linear |
| Extrusion width | 0.4 mm |
| Extruder temperature | 225°C |
| Perimeter shell | 1 |
| Layer height | 0.1 mm |
| Heated bed temperature | 50°C |
| Printing speed | 50 mm/s |

printing of the multi-material finger are summarized in Table II. The mass of the design model in Fig. 8(a) is calculated to be 15.1 g, while the mass of the two prototyped fingers is 16 g and 16.6 g, respectively. The manufacturing error is around 8% on average when 3D printing the fingers.

Two identical multi-material compliant fingers were installed on an electric gripper actuator (TOYO CHS25) to form an adaptive parallel gripper for grasping applications. To assess the adaptability of the parallel gripper, tests were conducted to evaluate its performance in grasping various shapes, including circular, rectangular, concave, and asymmetric objects printed with polylactic acid (PLA) material. During the tests, the objects were manually placed between the gripper fingers for grasping, with the fingertips pointed downward as shown in Fig. 9. The grasping points and positional errors can affect the adaptability and maximum payload of a gripper. The relative position between the fingers and objects was estimated visually to select gripping positions that maximize contact length, demonstrating possible optimal conditions for the grippers when grasping these objects.

The total contact length between the two fingers and the gripped object served as a metric for the gripper's adaptability. The results are presented in Fig. 9, with numerical values below each photo indicating the average total contact length from two tests. This measurement was determined using the open-source image processing and analysis program ImageJ. The program estimates the dimensions based on pixel count after setting a known reference distance in the image. By marking the contact region between the objects and the two fingers in the images shown in Fig. 9 using ImageJ, the total contact length can be obtained. Furthermore, these results were compared with the test outcomes obtained from commercially available fin ray-type compliant fingers (Festo adaptive gripper finger [31], DHAS-GF-80-U-BU) with a finger length of 80 mm, installed on the same gripper actuator, and our previously developed multi-phalange compliant gripper [15] operated through the bending motion of the compliant fingers.

Based on the results of the adaptability tests, it can be observed that the multi-material adaptive parallel gripper developed in this study exhibited a longer overall contact length when grasping objects of various shapes, making it more adaptable than the fin ray-type gripper and our previous gripper design operated through the bending motion of the compliant fingers. From the results of the two parallel driven grippers, it is noted that our innovative multi-material adaptive fingers can conform to all the shapes of the objects under consideration, unlike the fin ray-type

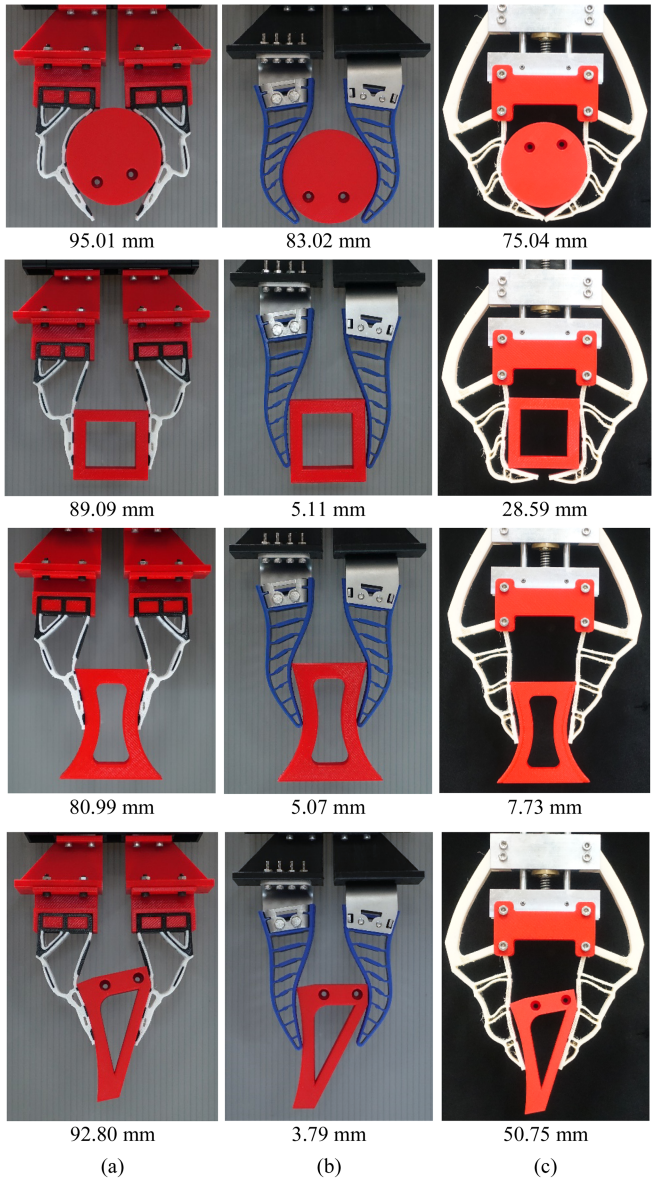


Fig. 9. Adaptability tests for grippers to grasp circular, rectangular, concave, and asymmetric objects. The numerical values below each photo indicates the average total contact length between both fingers and the object. (a) Multi-material adaptive parallel gripper. (b) Commercially available fin ray-type parallel gripper (Festo adaptive gripper finger, DHAS-GF-80-U-BU). (c) The multi-phalange gripper developed in [15] operated through the bending motion of the compliant fingers.

fingers which adapted well only to the shape of the circular object. The average total contact length of the multi-material adaptive parallel gripper when grasping circular, rectangular, concave, and asymmetric objects is respectively 1.14, 17.43, 15.97, and 24.49 times greater than that of the fin ray-type gripper design, and respectively 1.27, 3.12, 10.48, and 1.83 times greater than that of the multi-phalange gripper design.

To estimate the maximum payload capacity of the multi-material adaptive parallel gripper in grasping various shapes, payload tests depicted in Fig. 10 were conducted, with numerical values below each photo indicating the average maximum payload from two tests. These experiments involved gradually

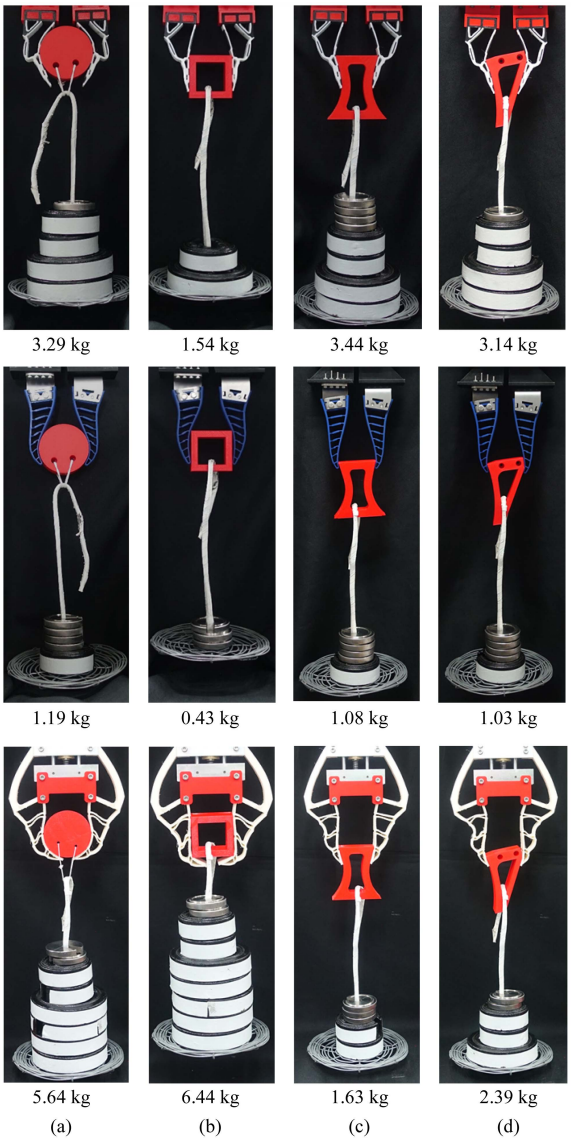


Fig. 10. Test results of the average maximum payload using the multi-material adaptive parallel gripper, the commercially available fin ray-type parallel gripper (Festo adaptive gripper finger, DHAS-GF-80-U-BU), and the multi-phalange gripper developed in [15] operated through the bending motion of the compliant fingers. The numerical values below each photo indicates the average maximum payload. (a) Circular object. (b) Rectangular object. (c) Concave object. (d) Asymmetric object.

increasing the weight plates on the tray hung from the gripped objects. The weight plates used included 100 g, 500 g, and 1000 g. When five 100 g weight plates can be steadily gripped, they are replaced with one 500 g weight plate, after which the weight is further increased until the object drops from the gripper. Then, the total load, including the weight of the gripped object, tray, and weight plates, was placed onto a digital weighing scale to measure the load. The maximum load capacity of the multi-material parallel gripper varies depending on the shape of the grasped object. The results indicated that the multi-material parallel gripper achieved maximum load capacities of 3.29 kg, 1.54 kg, 3.44 kg, and 3.14 kg on average when gripping the circular, rectangular, concave, and asymmetric objects, respectively.

Additionally, these payload test results are compared with the outcomes obtained from the commercially available fin ray-type parallel gripper and our previously developed multi-phalange compliant gripper [15]. The experimental results indicated that the average maximum payload capacities of the multi-material adaptive parallel gripper when gripping the circular, rectangular, concave, and asymmetric objects exceeded those of the fin ray-type compliant gripper by factors of 2.76, 3.58, 3.19, and 3.05, respectively. Our previously developed multi-phalange compliant gripper demonstrated its excellent capability for carrying maximum payloads when gripping the circular and rectangular objects, benefiting from its driving method and longer finger length. However, the maximum payload capacities of the multi-material parallel gripper when gripping the concave and asymmetric objects are 2.11 and 1.31 times greater, respectively, than those of the multi-phalange gripper design. If we consider only the results of the fin ray-type compliant gripper itself, it shows that the highest load capacity occurs when grasping the circular object. However, when gripping the rectangular, concave, and asymmetric objects, its maximum load capacity is low due to its poor adaptability to these shapes, as shown in Fig. 9(b).

Increasing surface roughness [32] and the contact area between two surfaces lead to an increase in friction, thereby increasing the payload capacity of a gripper. To measure the coefficients of friction between the gripper fingers and the 3D-printed objects, measurements were performed using an inclined plane. This involved slowly increasing the angle of inclination ($\theta$) of the plane until the object just began to slide. The coefficient of friction can then be calculated using the tangent of the angle $\theta$. According to our tests, the coefficients of friction between the PLA material and the three types of gripper fingers, as shown in Fig. 10, were estimated to be 0.47, 0.45, and 0.6, respectively.

In summary, our multi-material parallel gripper offers enhanced adaptability and payload capacity for different object shapes due to its unique structure identified through our presented optimization method, as well as the use of multiple materials with varying stiffness and flexibility. According to our previous study [33], a compliant finger printed with a higher infill density or made of a material with a higher elastic modulus can provide a higher output force but also requires a larger input force to deform. By varying the harder and softer materials of different parts of the compliant finger, one can fine-tune and customize its performance characteristics. For example, areas requiring more rigidity can use a harder material, while areas needing more flexibility can use a softer material. Possible future research could involve varying the elastic moduli of the materials and adjusting the differences in physical properties between the multi-materials to investigate their effects on material layout in topology optimization and the gripper's performance.

## VI. Conclusion

This letter presents a highly adaptive multi-material compliant finger design for parallel-jaw grippers, capable of conforming to circular, rectangular, concave, and asymmetric objects. The gripper's adaptability was determined based on the total contact length between its fingers and the object being grasped. The

findings indicated that our novel multi-material parallel gripper outperformed the fin ray-type compliant gripper in both adaptability and maximum load capacity. While our multi-material parallel gripper demonstrated conformity to all four tested shapes, the fin ray-type parallel gripper showed proficiency only with the circular object. By contrast, the multi-material parallel gripper developed in this study achieved a notable improvement in adaptability, outperforming the fin ray-type gripper by 19.3 times more on average in conforming to rectangular, concave, and asymmetric objects. As the adaptability of the gripper increases, it will enhance the stability of the grasping, produce a more uniform distribution of gripping force, and increase the maximum load capacity of the gripper.

The maximum load capacity of the multi-material parallel gripper varies depending on the shape of the grasped object. Our gripper achieved a maximum load capacity of 3.44 kg when gripping the concave object. Moreover, when grasping circular, rectangular, concave, and asymmetric objects, the maximum payload capacities of the multi-material parallel gripper exceed those of the fin ray-type parallel gripper by factors of 2.76, 3.58, 3.19, and 3.05, respectively, with an average increase of 3.2 times.

The experimental results demonstrated that the multi-material parallel gripper benefited from a design based on the presented multi-objective topology optimization method. Additionally, the consideration of multiple materials offers greater design freedom during optimization, leading to improved performance. Our multi-material adaptive finger can be installed on parallel-jaw gripper actuators for robotic automation, enabling applications with unknown objects of irregular size and shape, while also providing improved adaptability and maximum payload compared to fin-ray type compliant grippers.

## REFERENCES


[1] L. Birglen and T. Schlicht, "A statistical review of industrial robotic grippers," *Robot. Comput.-Integr. Manuf.*, vol. 49, pp. 88–97, 2018.

[2] K. Tatemura and H. Dobashi, "Strategy for roller chain assembly with parallel jaw gripper," *IEEE Robot. Automat. Lett.*, vol. 5, no. 2, pp. 2435–2442, Apr. 2020.

[3] N. A. Piga and L. Natale, "Adaptive tactile force control in a parallel gripper with low positioning resolution," *IEEE Robot. Automat. Lett.*, vol. 8, no. 9, pp. 5544–5551, Sep. 2023.

[4] G. Xie, R. Holladay, L. Chin, and D. Rus, "In-hand manipulation with a simple belted parallel-jaw gripper," *IEEE Robot. Automat. Lett.*, vol. 9, no. 2, pp. 1334–1341, Feb. 2024.

[5] H. Zhang, Y. Wu, E. Demeester, and K. Kellens, "Big-net: Deep learning for grasping with a bio-inspired soft gripper," *IEEE Robot. Automat. Lett.*, vol. 8, no. 2, pp. 584–591, Feb. 2023.

[6] S. Phodapol, A. Harnkhamen, N. Asawalertsak, S. N. Gorb, and P. Manoonpong, "Insect tarsus-inspired compliant robotic gripper with soft adhesive pads for versatile and stable object grasping," *IEEE Robot. Automat. Lett.*, vol. 8, no. 5, pp. 2486–2493, May 2023.

[7] J. H. Shin, J. G. Park, D. I. Kim, and H. S. Yoon, "A universal soft gripper with the optimized fin ray finger," *Int. J. Precis. Eng. Manuf.-Green Technol.*, vol. 8, pp. 889–899, 2021.

[8] G. Chen et al., "Intrinsic contact sensing and object perception of an adaptive fin-ray gripper integrating compact deflection sensors," *IEEE Trans. Robot.*, vol. 39, no. 6, pp. 4482–4499, Dec. 2023.

[9] J. Yao, Y. Fang, X. Yang, P. Wang, and L. Li, "Design optimization of soft robotic fingers biologically inspired by the fin ray effect with intrinsic force sensing," *Mechanism Mach. Theory*, vol. 191, 2024, Art. no. 105472.

[10] C.-H. Liu et al., "Optimal design of a soft robotic gripper for grasping unknown objects," *Soft Robot.*, vol. 5, no. 4, pp. 452–465, 2018.

[11] Y. Chen, Z. Xia, and Q. Zhao, "Optimal design of soft pneumatic bending actuators subjected to design-dependent pressure loads," *IEEE/ASME Trans. Mechatronics*, vol. 24, no. 6, pp. 2873–2884, Dec. 2019.

[12] C.-H. Liu, L.-J. Chen, J.-C. Chi, and J.-Y. Wu, "Topology optimization design and experiment of a soft pneumatic bending actuator for grasping applications," *IEEE Robot. Automat. Lett.*, vol. 7, no. 2, pp. 2086–2093, Apr. 2022.

[13] C.-H. Liu, Y. Chen, and S.-Y. Yang, "Topology optimization and prototype of a multimaterial-like compliant finger by varying the infill density in 3D printing," *Soft Robot.*, vol. 9, no. 5, pp. 837–849, 2022.

[14] J. Huang, Z. Wei, Y. Cui, and J. Liu, "Clamping force manipulation in 2D compliant gripper topology optimization under frictionless contact," *Struct. Multidisciplinary Optim.*, vol. 66, no. 7, 2023, Art. no. 164.

[15] C.-H. Liu, S.-Y. Yang, and Y.-C. Shih, "Optimal design of a highly self-adaptive gripper with multi-phalange compliant fingers for grasping irregularly shaped objects," *IEEE Robot. Automat. Lett.*, vol. 8, no. 11, pp. 7026–7033, Nov. 2023.

[16] J. Pinskier et al., "Diversity-based topology optimization of soft robotic grippers," *Adv. Intell. Syst.*, vol. 6, 2024, Art. no. 2300505.

[17] L. Y. Lee, O. A. Syadiqeen, C. P. Tan, and S. G. Nurzaman, "Closed-structure compliant gripper with morphologically optimized multi-material fingertips for aerial grasping," *IEEE Robot. Automat. Lett.*, vol. 6, no. 2, pp. 887–894, Apr. 2021.

[18] J. Shintake, V. Cacucciolo, D. Floreano, and H. Shea, "Soft robotic grippers," *Adv. Mater.*, vol. 30, no. 29, 2018, Art. no. 1707035.

[19] K. Blanco, E. Navas, L. Emmi, and R. Fernández, "Manufacturing of 3D printed soft grippers: A review," *IEEE Access*, vol. 12, pp. 30434–30451, 2024.

[20] B. Zhu et al., "Design of compliant mechanisms using continuum topology optimization: A review," *Mechanism Mach. Theory*, vol. 143, 2020, Art. no. 103622.

[21] J. Wu, O. Sigmund, and J. P. Groen, "Topology optimization of multi-scale structures: A review," *Struct. Multidisciplinary Optim.*, vol. 63, pp. 1455–1480, 2021.

[22] A. T. Gaynor, N. A. Meisel, C. B. Williams, and J. K. Guest, "Multiple-material topology optimization of compliant mechanisms created via PolyJet three-dimensional printing," *ASME J. Manuf. Sci. Eng.*, vol. 136, no. 6, 2014, Art. no. 061015.

[23] M. P. Bendsøe and O. Sigmund, "Material interpolation schemes in topology optimization," *Arch. Appl. Mechanics*, vol. 69, pp. 635–654, 1999.

[24] W. Zuo and K. Saitou, "Multi-material topology optimization using ordered SIMP interpolation," *Struct. Multidisciplinary Optim.*, vol. 55, no. 2, pp. 477–491, 2017.

[25] O. A. A. da Silveira and L. F. Palma, "Some considerations on multi-material topology optimization using ordered SIMP," *Struct. Multidisciplinary Optim.*, vol. 65, 2022, Art. no. 261.

[26] O. Sigmund, "Manufacturing tolerant topology optimization," *Acta Mechanica Sinica*, vol. 25, no. 2, pp. 227–239, 2009.

[27] K. Svanberg, "The method of moving asymptotes—A new method for structural optimization," *Int. J. Numer. Methods Eng.*, vol. 24, no. 2, pp. 359–373, 1987.

[28] B. J. Hancock and C. A. Mattson, "The smart normal constraint method for directly generating a smart Pareto set," *Struct. Multidisciplinary Optim.*, vol. 48, no. 4, pp. 763–775, 2013.

[29] D. J. Munk, T. Kipouros, G. A. Vio, G. T. Parks, and G. P. Steven, "Multiobjective and multi-physics topology optimization using an updated smart normal constraint bi-directional evolutionary structural optimization method," *Struct. Multidisciplinary Optim.*, vol. 57, no. 2, pp. 665–688, 2018.

[30] C.-H. Liu, Y. Chen, and S.-Y. Yang, "Quantification of hyperelastic material parameters for a 3D-printed thermoplastic elastomer with different infill percentages," *Mater. Today Commun.*, vol. 26, 2021, Art. no. 101895.

[31] [Online]. Available: https://festo.com/

[32] C.-H. Liu, C.-H. Chiu, M.-C. Hsu, Y. Chen, and Y.-P. Chiang, "Topology and size–shape optimization of an adaptive compliant gripper with high mechanical advantage for grasping irregular objects," *Robotica*, vol. 37, no. 8, pp. 1383–1400, 2019.

[33] C.-H. Liu and P.-T. Hung, "Effect of the infill density on the performance of a 3D-printed compliant finger," *Mater. Des.*, vol. 223, 2022, Art. no. 111203.